Surface and Near-Surface Engineering of PtCo Nanowires at Atomic Scale for Enhanced Electrochemical Sensing and Catalysis

Mingchuan Luo,[†,¶] Yingjun Sun,[†,‡,¶] Yingnan Qin,[†,‡] Shulin Chen,[§] Yingjie Li,[†] Chunji Li,[†] Yong Yang,[†] Dong Wu,[†] Nuoyan Xu,[†] Yi Xing,[†] Lei Wang,[‡] Peng Gao,[§,∥] and Shaojun Guo*[,†,⊥,#]

[†]Department of Materials Science & Engineering, College of Engineering, Peking University, Beijing 100871, China

[‡]College of Chemistry and Molecular Engineering, Qingdao University of Science and Technology, Qingdao 266042, China

[§]Electron Microscopy Laboratory, and International Center for Quantum Materials, School of Physics, Peking University, Beijing 100871, China

[∥]Collaborative Innovation Centre of Quantum Matter, Beijing 100871, China

[⊥]BIC-ESAT, College of Engineering, Peking University, Beijing 100871, China

[#]Department of Energy and Resources Engineering, College of Engineering, Peking University, Beijing 100871, China

Ⓢ *Supporting Information*

ABSTRACT: Among the most efficient strategies to boost the electrochemical sensing and catalysis of Pt-based multimetallic nano-materials is atomically manipulating the surface and near-surface nanostructures, which directly govern the adsorption behavior. Using one-dimensional PtCo urchin-like nanowires as the platform, we herein achieve the construction of high-index faceted Pt-skin configuration. Such unique structure shows excellent electrocatalytic performance toward the electrochemical detection of various molecules (H_2O_2, NH_2NH_2, dopamine, and acetaminophen), with the capability of real-time monitoring of H_2O_2 released from living cells and an impressive detection limit of 0.4 nM. Meanwhile, the combination of high-index facet and Pt-skin architecture also enables enhanced catalytic activity for the electro-reduction of oxygen in acid, realizing a very high mass activity of 2.2 A/mg_{Pt}. Our study demonstrates the great potential of surface and near-surface engineering at the atomic level in promoting the electrocatalysis on multimetallic nanomaterials for electrochemical sensors and renewable energy technologies.
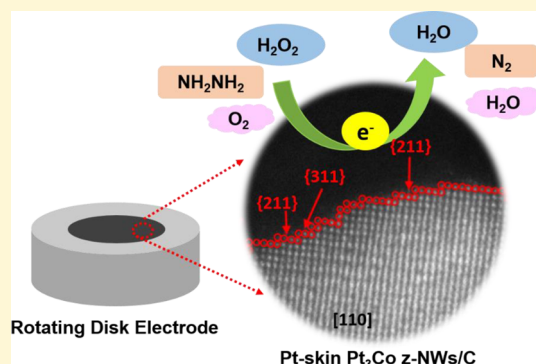
INTRODUCTION

The practical adoption of numerous electrochemistry-based technological innovations critically depends on the operative efficiency of electrocatalysis at solid−liquid interfaces and experimentally on the applied electrocatalytic materials.[1−3] Multimetallic nanomaterials have shown great promise in electrocatalysis due to their unique physicochemical properties, such as good electronic conductivity, excellent catalytic activity, and stability.[4−7] In the past few decades, much progress has been achieved in tuning the compositions, sizes, morphologies, and architectures of multimetallic nanomaterials at nanoscale for the enhanced electrocatalytic performance.[8−23] However, electrocatalysis is principally a heterogeneous process, in which only the surface and near-surface (a few atomic layers below surface) properties of the used electrocatalysts govern the resulting catalytic activity.[20] Therefore, it would be more efficient to directly tune the atomic structures of the surface and near-surface to achieve desired activity enhancement.

For highly crystalline metals, depending on the coordination numbers of surface atoms and their arrangements, the exposed surfaces are usually classified as low- and high-index facets.[24]

Recent studies showed that the high density of atomic steps, ledges, and kinks on high-index facets (HIFs) facilitated the activation of reactant molecules, thus leading to considerably higher electrocatalytic activity over the low index facets (LIFs).[25−27] For example, Sun and co-workers synthesized high-index faceted tetrahexahedral Pt nanocrystals with an electrochemical approach, which showed 4 times activity enhancement relative to the low-index faceted Pt nanospheres toward the electro-oxidation of small organic fuels.[28] On the other hand, the spatial distributions of elements at the atomic level in the near-surface region also strongly impact the catalytic properties of the outermost atoms via the ligand and/or strain effect.[29−31] By constructing a "sandwich structure" Pt skin via atomic level segregation on Pt_3Ni single-crystalline surface, Marković and co-workers achieved an impressive activity enhancement for oxygen reduction reaction (ORR) by nearly 2 orders of magnitude than the benchmark Pt/C catalyst.[32,33] Despite of the obvious advantages, it remains a
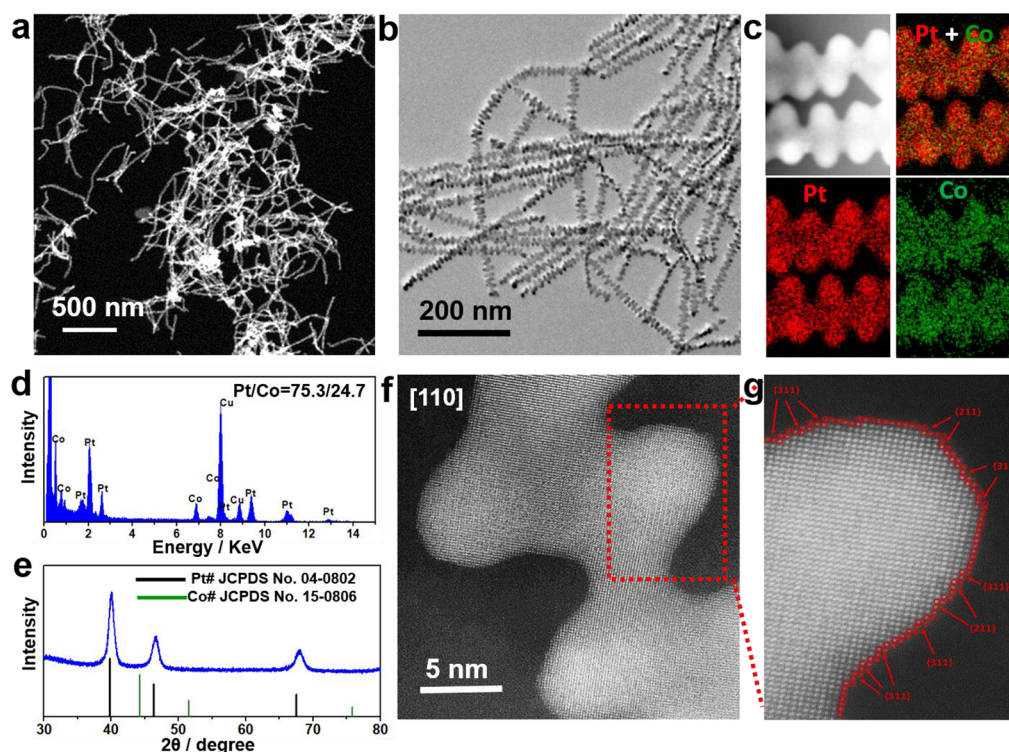
Figure 1. Representative (a) HAADF-STEM image, (b) TEM image, (c) STEM-EDS elemental mapping, (d) TEM-EDS, (e) XRD pattern, and (f, g) atomic HAADF-STEM image of as-synthesized Pt₃Co z-NWs.

grand challenge to transfer the above-mentioned desired catalytic surface and near-surface on multimetallic nanomaterials due to their intrinsically unfavorable thermodynamics.

To address this challenge, we herein presented a facile synthetic route that enables the simultaneously atomic-level tuning of surface and near-surface structures by constructing high-index faceted Pt-skin on Pt₃Co zigzag nanowires (z-NWs). Using the electrochemical detection of H_2O_2 as a probe, we found the Pt-skin Pt₃Co z-NWs exhibit excellent electrocatalytic performance for H_2O_2 sensing, with a lowest detective limit reaching sub-nM level reported to date. These unique surface and near-surface features also facilitate the electrocatalytic detection of other chemical molecules, including NH_2NH_2, dopamine, and acetaminophen, rendering a universal and efficient electrocatalytic sensing platform. Moreover, the Pt-skin Pt₃Co z-NWs also exhibit an impressive ORR electrocatalytic activity that is 20 times higher than that of commercial Pt/C. Together, this work advances the structural modification of Pt-based electrocatalytic nanomaterials to atomic level in the surface and near-surface region, which opens a new avenue for the design and synthesis of more efficient electrocatalysts for electrochemical sensors and energy converting devices.

■ EXPERIMENTAL SECTION

Chemicals. Platinum acetylacetonate ($Pt(acac)_2$), cobalt acetylacetonate ($Co(acac)_3$), oleylamine (OAm), hexadecylammonium chloride (CTAC), and *N*-formylmethionyl-leucyl-phenylalanine (fMLP) were all purchased from Sigma-Aldrich. Isopropanol and L-ascorbic acid (L-AA) were obtained from J&K Scientific. Pt/C catalyst (20 wt %) was obtained from Johnson-Matthey Corp. Cyclohexane, ethanol, ammonia solution (25 wt %), hydrazine hydrate (NH_2NH_2), hydrogen peroxide (H_2O_2), dopamine (DA), and acetaminophen (APAP) were supplied by Beijing Tongguang Fine Chemicals Company. Sodium dihydrogen phosphate

(NaH_2PO_4), disodium hydrogen phosphate (Na_2HPO_4), sodium chloride (NaCl), and sodium sulfide (Na_2SO_4) were provided by Xilong Chemical Factory. Nafion solution (5 wt %) was bought from Alfa Aesar, and *N,N*-dimethylformamide (DMF) was purchased from Tianjin Kangkede technology Co, Ltd. Fructose (FRU), glucose (GLU), and uric acid (UA) were obtained from Sinopharm Chemical Regent Co, Ltd. All chemicals were used without further purification and all solutions were freshly prepared with ultrapure water (18.2 MΩ/cm).

Materials Preparation. *Synthesis of Pt₃Co Zigzag Nanowires.* In a typical synthesis of Pt₃Co nanowires, $Pt(acac)_2$ (10 mg), $Co(acac)_3$ (6 mg), glucose (20 mg), and CTAC (40 mg) were mixed with 5 mL of OAm in a vial, followed by sonicating for 30 min and preheating at 65 °C in oil bath for 40 min. Subsequently, the temperature was raised to 200 °C and kept for 12 h. The final colloidal products were collected by centrifugation at 5500 rpm/min for 5 min after cooling down to room temperature. After washing with ethanol/cyclohexane mixture for three times, the Pt₃Co nanowires were redispersed in 10 mL of cyclohexane for further use.

Preparation of Pt₃Co Zigzag Nanowires/C and Pt-Skin Pt₃Co Zigzag Nanowires/C. The Pt₃Co zigzag nanowires/C catalyst was prepared as follows: 10 mL of Pt₃Co zigzag nanowires (0.7 mg/mL) cyclohexane solution was mixed with 10 mL of ethanol dispersed carbon (1.5 mg/mL) under sonication for 1 h. Subsequently, the products were collected by centrifugation at 6000 rpm for 5 min and drying at ambient condition overnight. The residual OAm on nanocrystals was removed by thermal annealing at 220 °C for 1.5 h in an oven. To obtain the Pt-skinned sample, the as-obtained Pt₃Co zigzag nanowires/C was placed at 400 °C for 2 h under N_2 atmosphere to induce near-surface compositional segregation.

Apparatus. Transmission electron microscopy (TEM) images were taken from a Tecani-G2 T20 operating at 200 kV, and high-resolution TEM (HRTEM) was carried out on a FEI Tecnai-G2 F30 at 300 kV. HAAD-STEM images and STEM-EDS elemental mapping analysis were taken from a JEOL-2100F transmission electron microscope at an acceleration voltage of 300 kV. The samples were prepared by dropping their cyclohexane dispersion onto the carbon-coated copper TEM grids using pipettes and dried under ambient condition. The

compositions of catalysts were determined by the inductively coupled plasma−atomic emission spectroscopy (ICP-AES, Agilent 8800). XRD patterns were collected using an X'Pert-Pro X-ray powder diffractometer equipped with a Cu radiation source (λ = 0.15406 nm).

Electroanalytical and Electrocatalytic Tests. The catalyst ink was prepared by sonicating each catalyst powder into a mixture of water, isopropanol, and Nafion solution (v/v/v = 1/1/0.025), giving rise to a concentration of 1 mg/mL. All electrochemical tests were conducted on a CHI760e electrochemical workstation (Shanghai Chenhua Instrument Corporation, China) in a conventional three-compartment cell by using a glass-carbon rotating disk electrode (RDE, 5 mm in diameter, 0.196 cm^2 in geometric area) as the working electrode. A platinum wire and Ag/AgCl electrode was used as the counter and reference electrode, respectively. The potential values were given with respect to the reversible hydrogen electrode (RHE), which were calculated from the potential of the Ag/AgCl electrode by $E_{RHE} = E_{Ag/AgCl} + 0.197 V + 0.059 \times pH$. Based on ICP-AES measurement, the loading amounts of Pt for the commercial Pt/C, Pt$_3$Co/C, and Pt-skin Pt$_3$Co/C catalysts were determined to be 2.00, 1.15, and 1.10 μg, respectively.

The electrochemical detection for small molecules (H$_2$O$_2$, NH$_2$NH$_2$, DA, and APAP) was conducted in 0.05 M phosphate buffered saline solution (PBS, pH = 7.4). The specific area-normalized CVs were recorded between −0.6 or 0 and 0.6 V versus Ag/AgCl electrode at a scan rate of 50 mV s^{-1}. The chronoamperometric test was applied at a constant potential with a rotating rate of 300 rpm. Raw 264.7 cells were purchased from China Infrastructure of Cell Line Resource. The cells were grown at 37 °C in 5% CO$_2$ in flasks, collected by centrifugation, and washed with PBS solutions three times before growing to 90% confluence. The number of the cells was counted by hemocytometer, and the final packed products were dispersed in 30 mL of PBS for the real-time electrochemical experiments at an applied potential of −0.05 V. The N-formylmethiony-leucy-phenylalanine (fMLP) was chosen as a stimulant to make the cells release H$_2$O$_2$ during the real-time detection process.

Cyclic voltammograms (CVs) were recorded in N$_2$-saturated 0.1 M HClO$_4$ at a scan rate of 50 mV s^{-1}, while CO stripping curves were recorded in N$_2$-saturated 0.1 M HClO$_4$ at a scan rate of 20 mV s^{-1} after the working electrodes were preadsorbed for 10 min. Electrochemically active surface areas (ECSAs) were calculated from the desorption charge of underpotentially deposited hydrogen (H$_{upd}$) assuming a charge density of 210 C/cm^2 for a monolayer of adsorbed hydrogen and the charge of CO stripping assuming a charge density of 420 C/cm^2 for a monolayer of adsorbed CO. The ORR polarization curves were recorded in O$_2$-saturated 0.1 M HClO$_4$ solution at a scan rate of 20 mV s^{-1} and a rotating rate of 1600 rpm. The kinetic currents were calculated from the Koutechy−Levich equation at 0.9 V versus RHE. Specific activity and mass activity were obtained by normalizing kinetic currents to corresponding ECSAs (from CO stripping) and Pt mass.

■ RESULTS AND DISCUSSION

Transmission electron microscopy (TEM) and aberration corrected scanning TEM (STEM) techniques were used to characterize the morphology and structure of as-obtained products. Low-magnification TEM images of as-synthesized Pt$_3$Co z-NWs reveal they have a high chemical yield of 100% (Figures 1a,b and S1 and S2). The elemental mapping of Pt$_3$Co z-NWs collected from STEM reveals the homogeneous distribution of Pt (red) and Co (green) through the whole NWs (Figure 1c). The resulting Pt/Co ratio, determined from TEM energy dispersive X-ray spectroscopy (TEM-EDX), was around 75.3/24.7 (Figure 1d), consistent with the result from inductively coupled plasma atomic emission spectroscopy (ICP-AES). Additionally, the crystalline structure was characterized by powder X-ray diffraction (PXRD), which

demonstrates the highly crystalline nature of as-synthesized Pt$_3$Co z-NWs with face-center-cubic (*fcc*) structure (Figure 1e).[34] The corresponding *fcc* peaks locate between those of pure Pt (JCPDS No. 04-0802) and pure Co (JCPDS No. 15-0806), suggesting the formation of alloy PtCo phase.[35] The high-magnification STEM image reveals that the exposed surface of NW was highly uneven and dominated by under-coordinated atoms, indicating the presence of high index facets rather than the most common low-index facets (Figure 1f,g).[36]

Before conducting thermal annealing to induce the Pt-skin structure, we first deposited as-synthesized Pt$_3$Co z-NWs onto carbon black (EC-300) to minimize undesired aggregation (Figure S3). A temperature of 400 °C was selected as the inducing temperature for Pt-skin in Pt$_3$Co z-NWs, for the sake of an optimal balance between surface segregation and nanocrystals sintering. The TEM image of annealed Pt$_3$Co z-NWs/C shows that one-dimensional nanocrystals remain highly dispersed on carbon support with negligible morphology and composition change (Figures 2a and S3). The PXRD pattern of the annealed sample shows an *fcc* structure identical to that of raw Pt$_3$Co z-NWs (Figure S4). Most importantly, the highly uneven surface and high-index facets was well maintained after thermal annealing, as confirmed by the spherical aberration corrected STEM images (Figure 2b,c). To
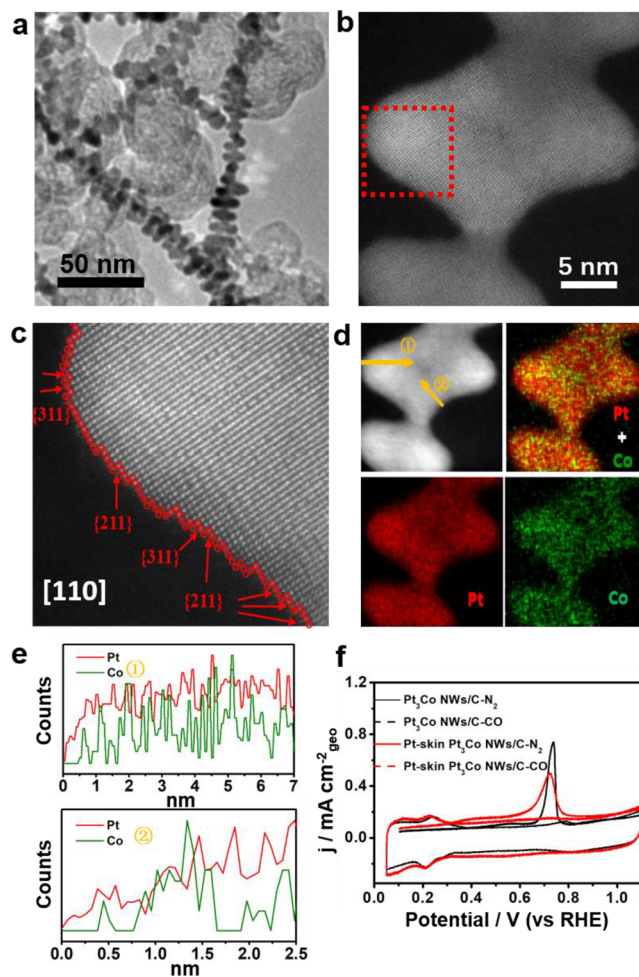

Figure 2. Representative (a) TEM image, (b, c) atomic resolution HAADF-STEM images, (d) STEM-EDS elemental mapping, (e) line scans, and (f) CO stripping profile of Pt-skin Pt$_3$Co z-NWs/C.
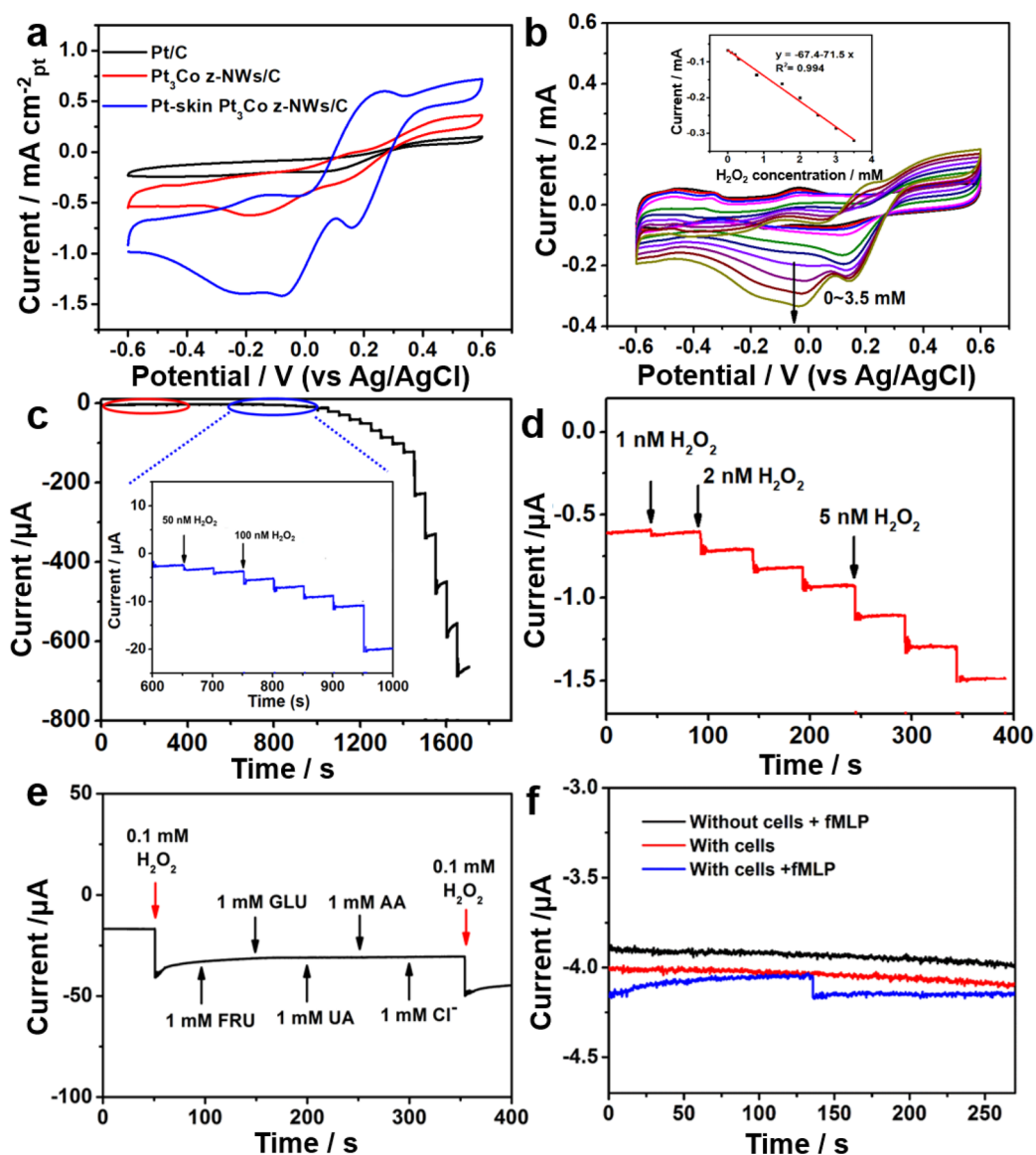
Figure 3. (a) CVs of various electrodes recorded in N_2-saturated 0.05 M PBS (pH = 7.4) solution containing 8 mM H_2O_2; scan rate 50 mV/s. (b) CVs of Pt-skin Pt_3Co z-NWs/C in N_2-saturated 0.05 M PBS (pH = 7.4) solution with different H_2O_2 concentrations. The inset shows the corresponding calibration curve. (c) The amperometric curve of Pt-skin Pt_3Co z-NWs/C electrode with continuous addition of H_2O_2; constant potential − 0.05 V. The inset shows the enlarged curve of the blue circled region. (d) The enlarged curve of the red circled region in (c). (e) The amperometric curve of Pt-skin Pt_3Co z-NWs/C electrode in N_2-saturated 0.05 M PBS with successive addition of 0.1 mM H_2O_2, 1 mM FRU, 1 mM GLU, 1 mM UA, 1 mM AA, and 1 mM Cl^-; constant potential −0.05 V. (f) The amperometric curves of Pt-skin Pt_3Co z-NWs/C electrode in the presence of either Raw 264.7 cells or fMLP and both.

reveal the elemental distribution of Pt and Co within the NWs, we further performed atomic resolution STEM elemental mapping (Figure 2d) and linear scan (Figure 2e), both of which confirm the existence of a pure Pt outer shell around an PtCo alloy inner core. The thickness of Pt-skin is measured to be around 0.5 nm, equal to two atomic layers of Pt.[15]

Surface-sensitive cyclic voltammograms (CVs) were recorded in N_2-saturated 0.1 M $HClO_4$ solution with and without CO preadsorption to characterize the distinctive surface and near-surface of Pt-skin Pt_3Co z-NWs. As shown in Figures 2f and S6, all catalysts display the typical electrochemical responses of Pt surface, namely, the underpotentially deposited hydrogen (H_{upd}) adsorption/desorption (0.075 to 0.4 V), double-layer region (0.4 to 0.7 V), and surface adsorption/reduction of hydroxyl species (0.7 to 1.1 V).[37] The

electrochemically active surface areas (ECSAs) of various catalysts were determined from the integrated charges of H_{upd} desorption ($ECSAH_{upd}$) and CO stripping (Table S1). The ratio of $ECSACO/ECSAH_{upd}$ for Pt-skin Pt_3Co z-NWs/C was 1.47, indicating the strong suppression of H_{upd} desorption on the surface and thus the formation of distinctive Pt-skin structure.[38] By contrast, the ratio for Pt_3Co z-NWs/C was 1.18, corresponding to a typical alloy surface. These electrochemical results in conjunction with the aberration corrected STEM, elemental mapping, and line scan collectively prove that the as-obtained Pt-skin Pt_3Co z-NWs possess the Pt-skin structure, along with exposed high index facets.

Using the electrocatalytic sensing of H_2O_2 as a probe, we examined the electroanalytical performance of our Pt-skin Pt_3Co z-NWs/C catalyst. Figure 3a shows the representative
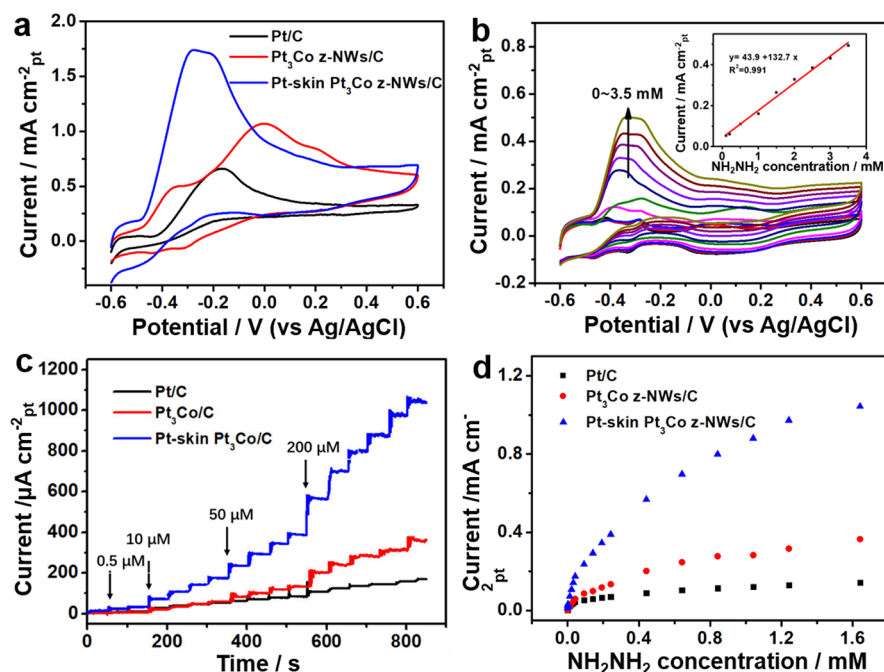
Figure 4. (a) CVs of various electrodes recorded in N_2-saturated 0.05 M PBS (pH = 7.4) solution containing 8 mM NH_2NH_2. (b) CVs of Pt-skin Pt_3Co z-NWs/C in N_2-saturated 0.05 M PBS (pH = 7.4) solution with different concentrations of NH_2NH_2. The inset shows the corresponding calibration curve. (c) The amperometric curves of various electrodes with continuous addition of NH_2NH_2 into PBS. (d) The detective current density dependence of various electrodes on the NH_2NH_2 concentration.]

CVs in N_2-saturated 0.05 M PBS (pH = 7.4) containing 8 mM H_2O_2. Impressively, the Pt-skin Pt_3Co z-NWs/C shows a peak current density of −1.47 mA cm^{-2} pt, around 3 and 8 times higher than the Pt_3Co z-NWs/C and commercial Pt/C, respectively, indicating its much enhanced H_2O_2 detective ability.[39] A good linear relationship can be established between the peak reduction current and H_2O_2 concentration (inset of Figure 3b) by recording CVs of Pt-skin Pt_3Co z-NWs/C in N_2-saturated 0.05 M PBS solution with H_2O_2 concentration from 0 to 3.5 mM (Figure 3b). Furthermore, both the anodic and cathodic currents are directly proportional to the square root of scan rates, suggesting the redox reaction is a typical diffusion-controlled electrochemical process (Figure S7). By studying the potential dependence of the current response, we further identified the optimized detective potential to be −0.05 V (Figure S8). Under this potential, the current response of 0.05 mM H_2O_2 on Pt-skin Pt_3Co z-NWs/C was 3.5 and 10.6 times higher than the values of Pt_3Co z-NWs/C and Pt/C, respectively (Figure S9).

Figure 3c shows the typical amperometric responses of the Pt-skin Pt_3Co/C z-NWs upon the injection of successive H_2O_2 into the 0.05 M PBS at a potential of −0.05 V. After each injection, the steady-state current could be achieved within 3 s. An enlarged image of a red circle in Figure 3c is shown in Figure 3d. Based on the signal-to-noise ratio (signal/noise = 3), the detection limit of Pt-skin Pt_3Co z-NWs/C for H_2O_2 can reach 0.4 nM, much lower than other reported advanced catalysts and HRP enzymes (Table S2). Figure S10 plots the recorded current as a function of H_2O_2 concentration, yielding three distinct linear relationships in the ranges of 1−50 nM (Figure S10b, R^2 = 0.996, sensitivity = 461.7 μA cm^{-2} $μM^{-1}$), 0.06−0.6 μM (Figure S10c, R^2 = 0.997, sensitivity = 233.7 μA cm^{-2} $μM^{-1}$), and 1.02−315 μM (Figure S10d, R^2 = 0.999, sensitivity = 30.3 μA cm^{-2} $μM^{-1}$). This phenomenon suggests the strong reaction kinetics dependence on H_2O_2 concen-

tration. At extremely low H_2O_2 concentration, the reactant adsorption was the rate-determining step, while at extremely high H_2O_2 concentration, the reaction was rate-limited by H_2O_2 activation.[40]

The anti-interference response of the Pt-skin Pt_3Co z-NWs/C electrode was studied by continuous addition of 0.1 mM H_2O_2 and 1 mM of other interferences (Figure 3e). There are almost no current changes upon the addition of 1 mM FRU, GLU, UA, AA, and Cl^-, indicating its high anti-interference capacity. The impressive selectivity of Pt-skin PtCo electrode can be mainly ascribed to its capability of electro-reducing H_2O_2 at a very negative potential, in which condition the electrochemical redox reactions of other interfering species rarely happens. The real-time monitoring performance of as-fabricated Pt-skin Pt_3Co z-NWs/C electrode was further checked by detecting H_2O_2 released from the Raw 264.7 cells. In this study, fMLP was selected as a stimulant for the cell to exude H_2O_2. As shown in Figure 3f, the cathodic current obviously changes after the injection of 0.3 μM fMLP in the presence of Raw 264.7 cells, corresponding to around 125 nM of H_2O_2 released from the living cells. Meanwhile, negligible current response can be observed in the absence of either fMLP or Raw 264.7 cells, indicating that the Pt-skin Pt_3Co z-NWs/C electrode can serve as an ultrahigh sensitive platform for H_2O_2 detection.

The electrochemical detection of NH_2NH_2 was also studied using Pt-skin Pt_3Co z-NWs/C, Pt_3Co z-NWs/C, and Pt/C as the electrocatalytic sensing nanomaterials. Pt-skin Pt_3Co z-NWs/C still shows enhanced current response in the presence of 8 mM NH_2NH_2 (Figure 4a), about 1.7 and 3 times higher than those Pt_3Co z-NWs/C and Pt/C, respectively, suggesting the promoting role of Pt-skin structure in the electrooxidation catalysis of NH_2NH_2. A good linear relationship can be obtained when the NH_2NH_2 concentration is increased from 0 to 3.5 mM according to the results of CVs (Figure 4b and the
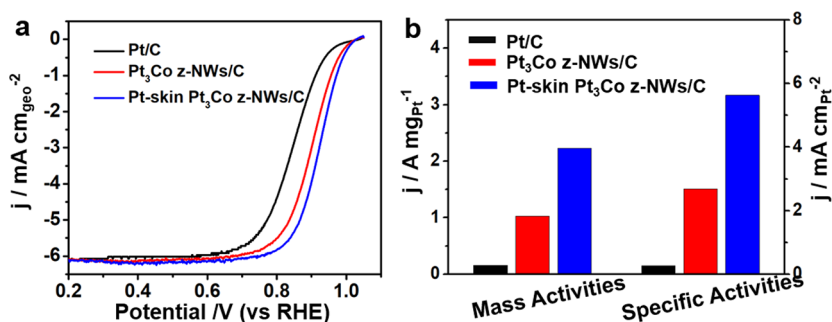
Figure 5. (a) ORR polarization curves and (b) ORR-specific activities and mass activities of Pt-skin Pt$_3$Co z-NWs/C, Pt$_3$Co z-NWs/C, and commercial Pt/C.

inset). When the scan rate increases from 50 to 500 mV/s, the peak currents increase linearly with the square root of the scan rate, indicating the oxidation of NH$_2$NH$_2$ on Pt-skin Pt$_3$Co/C is a typical diffusion-controlled process (Figure S11). Figure 4c shows the amperometric responses of different catalysts toward successive addition of hydrazine at an applied potential of −0.3 V. The Pt-skin Pt$_3$Co z-NWs/C has the largest current response toward NH$_2$NH$_2$ sensing. Figure 4d depicts the dependence of the responses of the different electrodes on NH$_2$NH$_2$, where the Pt-skin Pt$_3$Co electrode can achieve a wide linear range over the concentration of NH$_2$NH$_2$ from 0.5 to 42 μM with a high sensitivity as high as 3.76 mA cm^{-2} mM^{-1} (Figure S12) and from 42 μM to 1.6 mM with a detection sensitivity of 0.55 mA cm^{-2} mM^{-1} (Figure S12). The detection limit was calculated to be 0.1 μM (signal/noise = 3) (Figure S13), which was lower than most of the other reported materials (Table S3). The results indicate that the Pt-skin Pt$_3$Co z-NWs possess a superior sensing performance over Pt$_3$Co NWs. In addition to H$_2$O$_2$ and NH$_2$NH$_2$, the Pt-skin Pt$_3$Co z-NWs also showed enhanced electrochemically detective performance for dopamine and acetaminophen relative to raw Pt$_3$Co z-NWs and commercial Pt/C (Figure S14).

The electrocatalytic performance of ORR was determined from the polarization curves recorded in O$_2$-saturated 0.1 M HClO$_4$. Obviously, the ORR activity increased in the trend of Pt/C < Pt$_3$Co z-NWs/C < Pt-skin Pt$_3$Co z-NWs/C, as reflected by the onset or half-wave potentials (Figure 5a). To quantitatively compare the intrinsic activity, the specific activity (SA) at 0.9 V versus the reversible hydrogen electrode was calculated by normalizing the kinetic current to the ECSA$_{CO}$.[41] Surprisingly, the SA of Pt-skin Pt$_3$Co z-NWs/C reaches 5.6 mA cm^{-2}, 2.1 and 20.7 times higher than those of Pt$_3$Co z-NWs/C and Pt/C, respectively. Pt-skin Pt$_3$Co z-NWs/C shows a Tafel slope of 76.8 mV decade^{-1}, lower than those of Pt$_3$Co z-NWs/C (88.6 mV decade^{-1}) and commercial Pt/C (93.4 mV decade^{-1}), suggesting its faster kinetics toward ORR (Figure S15a). The electron transfer number on Pt-skin Pt$_3$Co z-NWs/C is determined to be ~4 using the rotating ring disk electrode (Figure S15b,c). Moreover, Pt-skin Pt$_3$Co z-NWs/C also shows the highest mass activity (2.2 A/mg$_{Pt}$), 5 times over that of the 2020 U.S. Department of Energy target (0.44 A/mg$_{Pt}$) (Figure 5b)[42] and much higher than most of the reported Pt-based materials (Table S4). The Pt-skin Pt$_3$Co z-NWs/C also shows excellent stability, revealed by the fact that the specific and mass activities decrease by only 21.9% and 21.6%, respectively, after 50 000 potential cycles (Figure S15d). Together, the dramatic enhancement in ORR activity

of Pt-skin Pt$_3$Co z-NWs/C highlights the beneficial role of atomic level structural engineering on the surface and near-surface in enhancing electroanalytical and electrocatalytic applications.

CONCLUSIONS

In summary, we simultaneously controlled the exposed atomic arrangement on the surface and the spatial elemental distributions in the near-surface region on one-dimensional Pt$_3$Co NWs, leading to a catalytically desired high-index faceted Pt-skin configuration. The as-obtained Pt-skin Pt$_3$Co z-NWs not only serve as a universal and efficient electrochemical sensing platform toward various chemical molecules, including H$_2$O$_2$, NH$_2$NH$_2$, dopamine, and acetaminophen, but also exhibit excellent electrocatalytic activity toward ORR in acidic environment. The structure−performance relationship has been clearly established. This work highlights the importance of optimizing both the surface geometry and the near-surface architecture at the atomic level for enhanced electrocatalysis. Our design strategies can be generally applied to other multimetallic nanomaterials with different compositions and structures for electrochemistry-based applications.

ASSOCIATED CONTENT

ⓢ Supporting Information

The Supporting Information is available free of charge on the ACS Publications website at DOI: 10.1021/acs.chemmater.8b01638.

> Optimized experimental characterization information containing TEM images, TEM-EDS images, EDS-mapping image, line-scan image, XRD, and additional graphical information on electroanalysis and electrocatalytic measurement (PDF)

AUTHOR INFORMATION

Corresponding Author

*(S.G.) E-mail: guosj@pku.edu.cn.

ORCID ⓘ

Lei Wang: 0000-0001-7275-4846

Shaojun Guo: 0000-0003-4427-6837

Author Contributions

¶(M.L. and Y.S.) These authors contributed equally to this work.

Notes

The authors declare no competing financial interest.

■ REFERENCES

(1) Stamenkovic, V. R.; Strmcnik, D.; Lopes, P. P.; Markovic, N. M. Energy and Fuels from Electrochemical Interfaces. *Nat. Mater.* **2017**, *16*, 57−69.

(2) Seh, Z. W.; Kibsgaard, J.; Dickens, C. F.; Chorkendorff, I. B.; Nørskov, J. K.; Jaramillo, T. F. Combining Theory and Experiment in Electrocatalysis: Insights into Materials Design. *Science* **2017**, *355* (6321), eaad4998.

(3) Markovic, N. M. Electrocatalysis: Interfacing Electrochemistry. *Nat. Mater.* **2013**, *12*, 101−102.

(4) Gilroy, K. D.; Ruditskiy, A.; Peng, H. C.; Qin, D.; Xia, Y. Bimetallic Nanocrystals: Syntheses, Properties, and Applications. *Chem. Rev.* **2016**, *116*, 10414−10472.

(5) Wang, Y. J.; Zhao, N.; Fang, B.; Li, H.; Bi, X. T.; Wang, H. Carbon-Supported Pt-Based Alloy Electrocatalysts for the Oxygen Reduction Reaction in Polymer Electrolyte Membrane Fuel Cells: Particle Size, Shape, and Composition Manipulation and Their Impact to Activity. *Chem. Rev.* **2015**, *115*, 3433−3467.

(6) Yu, W.; Porosoff, M. D.; Chen, J. G. Review of Pt-Based Bimetallic Catalysis: from Model Surfaces to Supported Catalysts. *Chem. Rev.* **2012**, *112*, 5780−5817.

(7) Wang, D.; Peng, Q.; Li, Y. Nanocrystalline Intermetallics and Alloys. *Nano Res.* **2010**, *3*, 574−580.

(8) Luo, M.; Sun, Y.; Wang, L.; Guo, S. Tuning Multimetallic Ordered Intermetallic Nanocrystals for Efficient Energy Electrocatalysis. *Adv. Energy. Mater.* **2017**, *7*, 1602073−1602086.

(9) Sheng, T.; Xu, Y. F.; Jiang, Y. X.; Huang, L.; Tian, N.; Zhou, Z. Y.; Sun, S. G.; Broadwell, I. Structure Design and Performance Tuning of Nanomaterials for Electrochemical Energy Conversion and Storage. *Acc. Chem. Res.* **2016**, *49*, 2569−2577.

(10) Shao, M.; Chang, Q.; Dodelet, J. P.; Chenitz, R. Recent Advances in Electrocatalysts for Oxygen Reduction Reaction. *Chem. Rev.* **2016**, *116*, 3594−3657.

(11) Escudero-Escribano, M.; Malacrida, P.; Hansen, M. H.; Vej-Hansen, U. G.; Velázquez-Palenzuela, A.; Tripkovic, V.; Chorkendorff, I.; Schiotz, J.; Rossmeisl, J.; Stephens, I. E. L. Tuning the Activity of Pt Alloy Electrocatalysts by Means of the Lanthanide Contraction. *Science* **2016**, *352*, 73−76.

(12) Bu, L.; Zhang, N.; Guo, S.; Zhang, X.; Li, J.; Yao, J.; Huang, X.; Wu, T.; Lu, G.; Ma, J.-Y.; Su, X. Biaxially Strained PtPb/Pt Core/Shell Nanoplate Boosts Oxygen Reduction Catalysis. *Science* **2016**, *354*, 1410−1414.

(13) Zhang, L.; Roling, L. T.; Wang, X.; Vara, M.; Chi, M.; Liu, J.; Mavrikakis, M.; Choi, S.-I.; Park, J.; Herron, J. A.; et al. Platinum-Based Nanocages with Subnanometer-Thick Walls and Well-Defined, Controllable Facets. *Science* **2015**, *349*, 412−416.

(14) Hernandez-Fernandez, P.; Masini, F.; McCarthy, D. N.; Strebel, C. E.; Friebel, D.; Deiana, D.; Nielsen, J. H.; Malacrida, P.; Nierhoff, A.; Bodin, A.; et al. Mass-Selected Nanoparticles of Pt$_x$y as Model Catalysts for Oxygen Electroreduction. *Nat. Chem.* **2014**, *6*, 732−738.

(15) Chen, C.; Kang, Y.; Huo, Z.; Zhu, Z.; Huang, W.; Xin, H. L.; Chi, M.; Snyder, J. D.; Li, D.; Herron, J. A.; et al. Highly Crystalline Multimetallic Nanoframes with Three-Dimensional Electrocatalytic Surfaces. *Science* **2014**, *343*, 1339−1343.

(16) Becknell, N.; Son, Y.; Kim, D.; Li, D.; Yu, Y.; Niu, Z.; Stamenkovic, V. R.; Lei, T.; Sneed, B. T.; More, K. L.; et al. Control of

Architecture in Rhombic Dodecahedral Pt−Ni Nanoframe Electrocatalysts. *J. Am. Chem. Soc.* **2017**, *139*, 11678−11681.

(17) Zhang, J.; Yang, H.; Martens, B.; Luo, Z.; Xu, D.; Wang, Y.; Fang, J.; Zou, S. Pt−Cu Nanoctahedra: Synthesis and Comparative Study with Nanocubes on Their Electrochemical Catalytic Performance. *Chem. Sci.* **2012**, *3*, 3302−3306.

(18) Strasser, P. Catalysts by Platonic design. *Science* **2015**, *349*, 379−380.

(19) Zhang, J.; Yang, H.; Fang, J.; Zou, S. Synthesis and Oxygen Reduction Activity of Shape-Controlled Pt$_3$Ni Nanopolyhedra. *Nano Lett.* **2010**, *10*, 638−644.

(20) Nørskov, J. K.; Bligaard, T.; Rossmeisl, J.; Christensen, C. H. Towards the Computational Design of Solid Catalysts. *Nat. Chem.* **2009**, *1*, 37−46.

(21) Fu, Q.; Li, H.; Ma, Si; Hu, B.; Yu, S. A Mixed-Solvent Route to Unique PtAuCu Ternary Nanotubes Templated from Cu Nanowires as Efficient Dual Electrocatalysts. *Sci. China. Mater.* **2016**, *59*, 112−121.

(22) Wang, L.; Jia, W.; Liu, X.; Li, J.; Titirici, M. Sulphur-Doped Ordered Mesoporous Carbon with Enhanced Electrocatalytic Activity for the Oxygen Reduction Reaction. *J. Energy Chem.* **2016**, *25*, 566−570.

(23) Wang, H.; Zhang, J.; Chen, Z.; Zhang, M.; Han, X.; Zhong, C.; Deng, Y.; Hu, W. Size-Controllable Synthesis and High-Performance Formic Acid Oxidation of Polycrystalline Pd Nanoparticles. *Rare Met.* **2017**, DOI: 10.1007/s12598-017-0947-0.

(24) Xia, Y.; Xiong, Y.; Lim, B.; Skrabalak, S. E. Shape-Controlled Synthesis of Metal Nanocrystals: Simple Chemistry Meets Complex Physics? *Angew. Chem., Int. Ed.* **2009**, *48*, 60−103.

(25) Zhou, Z. Y.; Tian, N.; Li, J. T.; Broadwell, I.; Sun, S. G. Nanomaterials of High Surface Energy with Exceptional Properties in Catalysis and Energy Storage. *Chem. Soc. Rev.* **2011**, *40*, 4167−4185.

(26) Fortunelli, A.; Goddard, W. A., III; Sementa, L.; Barcaro, G.; Negreiros, F. R.; Jaramillo-Botero, A. The Atomistic Origin of the Extraordinary Oxygen Reduction Activity of Pt$_3$Ni$_7$ Fuel Cell Catalysts. *Chem. Sci.* **2015**, *6*, 3915−3925.

(27) Li, M.; Zhao, Z.; Cheng, T.; Fortunelli, A.; Chen, C. Y.; Yu, R.; Zhu, E.; Zhang, Q.; Gu, L.; Merinov, B. V.; et al. Ultrafine Jagged Platinum Nanowires Enable Ultrahigh Mass Activity for the Oxygen Reduction Reaction. *Science* **2016**, *354*, 1414−1419.

(28) Tian, N.; Zhou, Z. Y.; Sun, S. G.; Ding, Y.; Wang, Z. L. Synthesis of Tetrahexahedral Platinum Nanocrystals with High-Index Facets and High Electro-Oxidation Activity. *Science* **2007**, *316*, 732−735.

(29) Luo, M.; Guo, S. Strain-Controlled Electrocatalysis on Multimetallic Nanomaterials. *Nat. Rev. Mater.* **2017**, *2*, 17059−17072.

(30) Stephens, I. E.; Bondarenko, A. S.; Perez-Alonso, F. J.; Calle-Vallejo, F.; Bech, L.; Johansson, T. P.; Chorkendorff, I.; Jepsen, A. K.; Frydendal, R.; Knudsen, B. P.; Rossmeisl, J. Tuning the Activity of Pt (111) for Oxygen Electroreduction by Subsurface Alloying. *J. Am. Chem. Soc.* **2011**, *133*, 5485−5491.

(31) Strasser, P.; Koh, S.; Anniyev, T.; Greeley, J.; More, K.; Yu, C.; Toney, M. F.; Liu, Z.; Kaya, S.; Nordlund, D.; et al. Lattice-Strain Control of the Activity in Dealloyed Core−Shell Fuel Cell Catalysts. *Nat. Chem.* **2010**, *2*, 454−460.

(32) Stamenkovic, V. R.; Fowler, B.; Mun, B. S.; Wang, G.; Ross, P. N.; Lucas, C. A.; Marković, N. M. Improved Oxygen Reduction Activity on Pt$_3$Ni (111) via Increased Surface Site Availability. *Science* **2007**, *315*, 493−497.

(33) Stamenkovic, V. R.; Mun, B. S.; Mayrhofer, K. J.; Ross, P. N.; Markovic, N. M. Effect of Surface Composition on Electronic Structure, Stability, and Electrocatalytic Properties of Pt-Transition Metal Alloys: Pt-Skin versus Pt-Skeleton Surfaces. *J. Am. Chem. Soc.* **2006**, *128*, 8813−8819.

(34) Wang, C.; Van der Vliet, D.; Chang, K. C.; You, H.; Strmcnik, D.; Schlueter, J. A.; Stamenkovic, V. R.; Markovic, N. M.; et al. Monodisperse Pt$_3$Co Nanoparticles as A Catalyst for the Oxygen Reduction Reaction: Size-Dependent Activity. *J. Phys. Chem. C* **2009**, *113*, 19365−19368.

(35) Wang, D.; Xin, H. L.; Hovden, R.; Wang, H.; Yu, Y.; Muller, D. A.; Abruña, H. D.; DiSalvo, F. J. Structurally Ordered Intermetallic Platinum−Cobalt Core−Shell Nanoparticles with Enhanced Activity and Stability as Oxygen Reduction Electrocatalysts. *Nat. Mater.* **2013**, *12*, 81−87.

(36) Bu, L.; Ding, J.; Guo, S.; Zhang, X.; Su, D.; Zhu, X.; Huang, X.; Yao, J.; Guo, J.; Lu, G. A General Method for Multimetallic Platinum Alloy Nanowires as Highly Active and Stable Oxygen Reduction Catalysts. *Adv. Mater.* **2015**, *27*, 7204−7212.

(37) Paulus, U. A.; Wokaun, A.; Scherer, G. G.; Schmidt, T. J.; Stamenkovic, V.; Markovic, N. M.; Ross, P. N. Oxygen Reduction on High Surface Area Pt-Based Alloy Catalysts in Comparison to Well Defined Smooth Bulk Alloy Electrodes. *Electrochim. Acta* **2002**, *47*, 3787−3798.

(38) Van der Vliet, D. F.; Wang, C.; Li, D.; Paulikas, A. P.; Greeley, J.; Rankin, R. B.; Stamenkovic, V. R.; Strmcnik, D.; Tripkovic, D.; Markovic, N. M.; et al. Unique Electrochemical Adsorption Properties of Pt-Skin Surfaces. *Angew. Chem., Int. Ed.* **2012**, *51*, 3139−3142.

(39) Sun, Y.; Luo, M.; Meng, X.; Xiang, J.; Wang, L.; Ren, Q.; Guo, S. Graphene/Intermetallic PtPb Nanoplates Composites for Boosting Electrochemical Detection of H_2O_2 Released from Cells. *Anal. Chem.* **2017**, *89*, 3761−3767.

(40) Sun, Y.; Luo, M.; Qin, Y.; Zhu, S.; Li, Y.; Xu, N.; Meng, X.; Ren, Q.; Wang, L.; Guo, S. Atomic-Thick PtNi Nanowires Assembled on Graphene for High-Sensitivity Extracellular Hydrogen Peroxide Sensors. *ACS Appl. Mater. Interfaces* **2017**, *9*, 34715−34721.

(41) Gasteiger, H. A.; Kocha, S. S.; Sompalli, B.; Wagner, F. T. Activity Benchmarks and Requirements for Pt, Pt-Alloy, and Non-Pt Oxygen Reduction Catalysts for Pemfcs. *Appl. Catal., B* **2005**, *56*, 9−35.

(42) Kongkanand, A.; Mathias, M. F. The Priority and Challenge of High-Power Performance of Low-Platinum Proton-Exchange Membrane Fuel Cells. *J. Phys. Chem. Lett.* **2016**, *7*, 1127−1137.